





RESEARCH ARTICLE

PLASMA PROCESSES
AND POLYMERS

Study of plasma parameters and gas heating in the voltage range of nondischarge to full-discharge in a methane-fed dielectric barrier discharge

Nima Pourali¹  | Khuettian Lai¹ | Joe Gregory¹  | Yuyan Gong¹ |
Volker Hessel^{1,2}  | Evgeny V. Rebrov^{1,2,3} 

¹School of Engineering, University of Warwick, Coventry, UK

²School of Chemical Engineering and Advanced Materials, The University of Adelaide, Adelaide, South Australia, Australia

³Department of Chemical Engineering and Chemistry, Eindhoven University of Technology, Eindhoven, The Netherlands

Correspondence

Nima Pourali, School of Engineering, University of Warwick, Coventry CV4 7AL, UK.

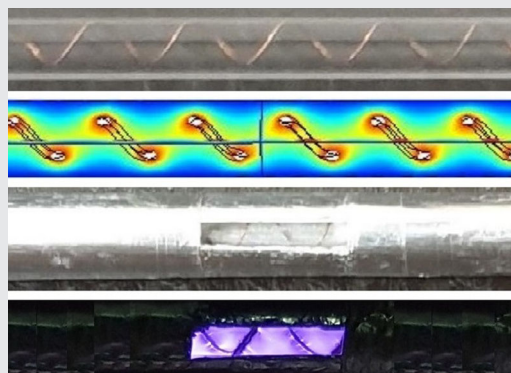
Email: Nima.Pourali@warwick.ac.uk

Funding information

H2020 European Research Council, Grant/Award Number: 810182

Abstract

Experimental data are used in theoretical models to study the effects of input voltage and gas flow rate on plasma and background gas parameters in a voltage range where the transition from nondischarge to full-discharge happens. To this end, a specific methane-fed dielectric barrier discharge is used as a plasma reactor, and electrical modeling, the Boltzmann equation method, and emission spectrum analysis are employed to calculate plasma parameters and gas heating. The output of this study proves that a uniform plasma with a controllable background gas heating is achievable by the adjustment of input parameters such as voltage and gas flow rate in a well-designed dielectric barrier discharge.



KEYWORDS

DBD, electrical measurement, electrical modeling, methane, OES

1 | INTRODUCTION

The strength of the C–H bond (434 kJ mol^{-1}) renders a significant threshold to overcome and has made methane conversion to value-added chemicals and targeted fuels a challenge of the last century^[1,2]. The chemical technologies developed in recent years for converting CH_4

include high-temperature catalytic processing, including oxidative coupling of methane and direct conversion of methane to heavier hydrocarbons like ethylene and acetylene^[3,4]. The use of nonthermal plasma technologies is an alternative route to tackle the barriers in CH_4 activation and conversion; as such plasma technology has recently generated increased interest for gas

This is an open access article under the terms of the Creative Commons Attribution License, which permits use, distribution and reproduction in any medium, provided the original work is properly cited.

© 2022 The Authors. *Plasma Processes and Polymers* published by Wiley-VCH GmbH.

processing^[5]. Among many procedures and sources to generate nonthermal plasmas, dielectric barrier discharge (DBD) in comparison to the other systems is useful because of considerably high specific power density, low gas consumption, and strong potential for upscaling^[6]. DBDs can operate at atmospheric pressure, which is most suitable for practical applications^[7]. Also, they are merged easily with catalytic packing materials, which opens new practical windows for the selective production of value-added compounds^[8]. In DBDs, when size of electrodes decreases the local electric field near them enhances. This local high electric field facilitates field emission of electrons and it increases secondary electron emission because of the accelerated ions. Also, the high reduced electric field creates a reactive atmosphere because electrons accelerate and collide energetically with other species, creating more reactive species. A high reduced electric field in a DBD generates high densities of charged particles at low values of specific deposited energy, which leads to higher energy efficiencies. In a conventional DBD system, the gas breakdown voltage is governed by Paschen's law which accounts for Townsend processes (electron impact ionization in the bulk of the plasma and secondary electron emission from the cathode)^[9]. However, in DBD system with electrodes having length scale of micrometers, field emission at the cathode can provide a significant source of electrons for ignition and sustenance of the plasma, leading to the reduction of the breakdown voltage and the formation of a self-sustained field emission-driven microdischarge^[10–12].

Plasma diagnostics techniques give information about the properties of a plasma^[13]. These techniques can considerably contribute toward the optimization of gas conversion^[14–18]. Electrical probes are the most accurate instruments to determine plasma power and obtain an in-depth understanding of the electrical properties of the discharge^[19–21]. For instance, the average gap voltage can be determined with great accuracy using electrical diagnostics, combined with a suitable equivalent circuit model^[22–24]. The ignition voltage determines the (reduced) electric field within the DBD plasma and is a key parameter for understanding the physics of plasma. The estimated reduced electric field can be used in the Boltzmann equation to determine the electron energy and electron density. Spectroscopic procedures for plasma diagnostics with the least perturbation study the emitted, absorbed, or dispersed radiation of plasma for the evolution of the plasma parameters and chemistry. Among the spectroscopic diagnosis of the gas phase, optical emission spectroscopy (OES) is very attractive because it is a noninvasive, in situ, easily implemented method, which is highly sensitive and easily

space-resolved. By using this method, parameters such as the excitation temperature, electron temperature, and electron density (based on the Stark broadening of atomic emission lines) can be determined^[25]. Also, it provides an estimation of the vibrational temperature of species and background gas temperature based on the rotational branch of spectral lines and information relating to the plasma chemistry and substances present in the plasma^[26]. Optical emission diagnosis of methane plasma has intensively been investigated in the literature^[27–31]. Bai et al. studied the reaction mechanism in nonthermal plasma-assisted methane conversion performed by different sources^[27]. They built a relationship between the relative optical emission intensity of free radicals and the distribution of key products, via both experimental measurement and reaction kinetics modeling. They found that the intensity ratio of C_2/CH , strongly dependent on the gas temperature, can be an important factor for the relative concentration of hydrocarbon products over a broad range of operating parameters. By the emission spectroscopy, Kado et al. reported that methane was highly dissociated to atomic carbon and hydrogen in spark discharge^[29]. The gas temperature in the spark discharge channel was as low as 420–460 K, calculated by the Boltzmann plot method of CH rotational band (431 nm). Akintola et al. analyzed N_2/CH_4 plasma by using OES and investigated products formed to characterize the effects of varying plasma parameters on product formation^[31]. This was done by determining relevant thermodynamic information such as electron density, vibrational, and rotational temperatures, as well as comparing the presence of key plasma species (C–N, C–H) to relevant products formed during nitrogen–methane coupling in plasma-alone and plasma catalytic reactions.

Although OES diagnostics and electrical measuring have been extensively reported in DBDs and especially for methane plasma in the literature, there is no research work that attempts to use data of OES and electrical probes to investigate effects of changing gas flow rate and voltage on background gas heating and plasma parameters. Therefore, this study is devoted to investigating the change of gas temperature, electric field, electron energy, and electron density resulting from the gas flow rate and applied voltage variations. This study considers a voltage range where transition from nondischarge to fully discharge operations happens. Also, a specific methane-fed DBD is used as plasma reactor and electrical modeling, Boltzmann equation method, and emission spectrum analysis are employed to calculate plasma parameters and gas heating. The paper is structured as follows: the next section describes the experimental setup and configuration of the reactor and explains the

electrical model, the results are discussed in Section 3, and finally, the last section gives a brief statement and conclusion of the paper.

2 | REACTOR STRUCTURE AND EXPERIMENTAL SETUP

A photograph of the DBD used in this study is presented in Figure 1. A quartz tube with dielectric constant 3.7 and inner and outer diameters of 3 and 5 mm, respectively was used as a dielectric barrier and container of discharge. The high voltage electrode was a copper spring with length 100 mm, outer diameter of 3 mm, wire thickness of 0.35 mm, and pitch of 5 mm. The ground electrode was aluminum foil tightly wrapped around the quartz tube with a length of 55 mm, it contained a rectangular optical window with a size of 2 mm × 7 mm.

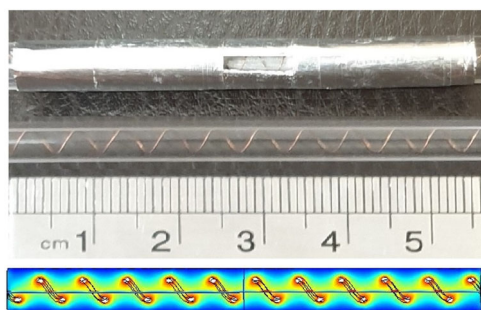


FIGURE 1 DBD structure

A schematic diagram of the experimental setup is presented in Figure 2, where the DBD was electrically powered by a G2000 High Voltage Plasma Generator (Redline Technologies). Sinusoidal wave voltages with a fixed frequency of 72 kHz and with different amplitudes were applied to the reactor. The reactor was fed with pure methane gas, whose flow was adjusted with a Bronkhorst mass flow controller. The applied voltage was measured with a 1000X High Voltage Probe (Tektronix P6015A), while a Rogowski coil (Pearson 6600) was used to measure the total current. An external capacitor (10 nF) was installed in the ground line to monitor the generated electric charges (Q) in the plasma. In addition, all electrical signals were recorded by PC oscilloscope (PicoScope 3000 Series, Picotech). The light emitted from the reactor was directly detected using an optical fiber positioned perpendicular to and placed 5 mm away from the reactor. A Princeton Instruments FERGIE Fiber Optic Spectrometer (FER-SCI-1024BX-UR) was used to record the emission spectra of the generated plasmas. This spectrometer is fitted with an integrated, deep cooled (-55°C absolute), back-illuminated 1024×256 CCD array for ultra-low noise with a grating of 1200 lines/mm and a 25 mm slit to give coverage over the range 200–1100 nm with ≈ 0.26 nm resolution. The gaseous products were analyzed online using a two-channel gas chromatograph (i.e., SHIMADZU 2010 Pro) with a thermal conductivity detector (TCD) and a flame ionization detector (FID). Two columns Rt-QS-BOND (RESTEC) and SH-Msieve 5A (SHIMADZU) were used for gases detection. The pressure and temperature of fed methane gas were fixed at ambient conditions. Methane

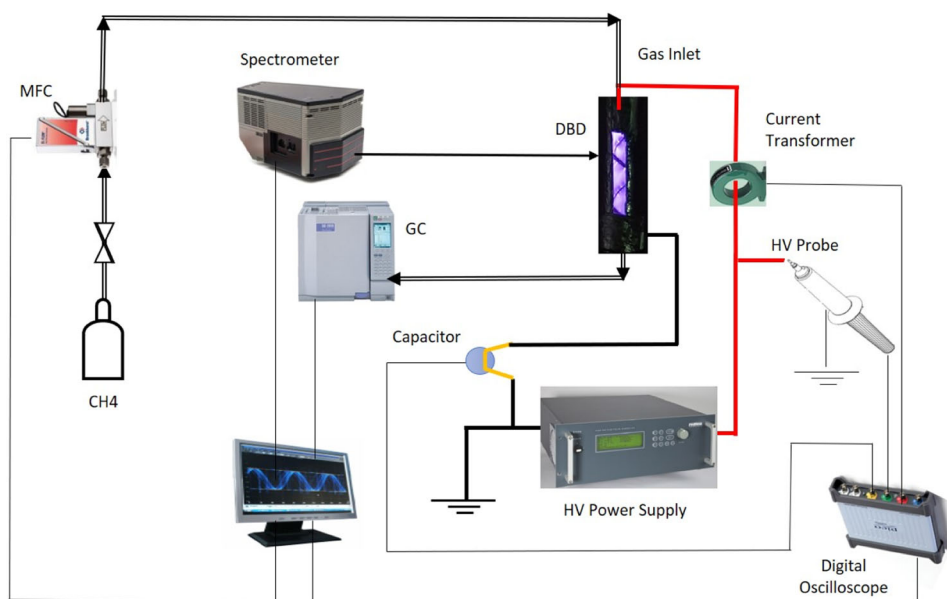


FIGURE 2 Schematic layout of the experimental setup

conversion is determined by gas chromatography (GC). GC was calibrated for methane and other product gases with different concentrations. When GC run it captures a definite volume of outlet mixture gas and determines the concentration of each species inside the mixture through calibration curves.

3 | RESULTS AND MODELING

This section presents the results of electrical modeling and measurements of the methane DBD as well as the results of OES diagnostics and analysis. The effects of applied voltage amplitude and gas flow on plasma parameters such as electron density, electron energy, electric field, electric charge, and background gas heating and conversion are discussed in this section.

3.1 | Electrical model and calculation of plasma parameters

Figure 3 is a schematic electrical diagram of the DBD in the experimental setup; the dashed rectangle represents the DBD reactor. C_g , C_b , and C_m are, respectively, gap capacitance, dielectric barrier capacitance, and external monitoring capacitance. Voltages across the plasma gap, dielectric barrier, and monitoring capacitor are denoted by V_p , V_b , and V_m , respectively. The net measured electric current is a combination of the displacement current (I_g) passing through the gap and plasma current (I_p) which is established when plasma is formed. The displacement current becomes zero when the plasma fills all gaps and the cell behaves as a conductor with a defined impedance. In a DBD both currents exist simultaneously because the gap area includes some nondischarge regions and the electrode area is split into nondischarging and discharging areas^[32]. Having defined the above parameters, Kirchhoff's circuit laws (voltage and current laws) can be applied to the circuit to calculate plasma voltage and plasma current:

$$V_p = V_s - V_m \left(1 + \frac{C_m}{C_b} \right), \quad (1)$$

$$I_p = I_m - C_g \frac{dV_s}{dt} + C_g \left(1 + \frac{C_m}{C_b} \right) \frac{dV_m}{dt}, \quad (2)$$

where V_s is the total voltage, measured as the output of the power supply connected to the high voltage electrode. The power consumed for plasma formation and discharge is equal to the output power of the plasma generator and can be calculated by:

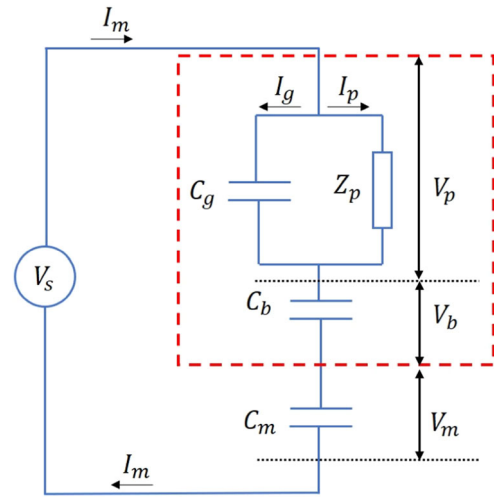


FIGURE 3 Equivalent electrical circuit diagram of the experimental setup; the dashed rectangle represents the DBD reactor.

$$P = \frac{1}{T} \int_0^T I_p V_p dt = \frac{1}{T} \int_0^T I_m V_s dt = \frac{1}{T} \int_0^T V_s dQ. \quad (3)$$

Notice the power consumed in a capacitor during an AC voltage period is zero. Having calculated I_p and V_p , one can also provide an estimation of the electric field, electron density, and electron energy. With having V_p and measured electrical charge the electric field in gap discharge E_g is determined by solving Poisson's equation in COMSOL Software. The reduced electric field is calculated by electric field and density of background gas in ambient condition. The relationship for the electron density is estimated as:

$$n_e = \kappa \frac{I_p}{e A_{in} E_g \mu_e}, \quad (4)$$

where e is elementary electric charge, A_{in} is the inner surface area of the dielectric barrier, and κ is the ratio of the electron current in the total electric current, set at 0.5 because the electron-ion pairs are formed by electron collision ionization and they have the same participation in plasma current. For the calculation of electron mobility, μ_e , and electron energy we used BOLSING+ software^[33] (see <http://www.lxcat.laplace.univ-tlse.fr> for a website to access BOLSING+) which is a free software for the numerical solution of the Boltzmann equation for electrons in weakly ionized gases). The website also includes electron-impact cross-sections of the different commonly used gases in plasma processing. This software calculates the transport coefficient, the rate constant and electron mean energy for each value of E/N from collision cross-section data by solving the

electron Boltzmann equation (two-term approximation). It means that cross-section data for each reaction must be inserted as an input parameter. Also, the gas temperature must initially be fixed. All cross-section data and reaction considered here for methane plasma are the same as data used in our previous works^[34,35]. Determining the C_b is straightforward and it is given by:

$$C_b = \frac{2\pi\epsilon_0\epsilon_b l}{\ln(r_{out}/r_{in})}, \quad (5)$$

which for a relative dielectric permittivity of 3.7 gives $C_b = 22.13$ pF. l is the length of the discharge region (same as ground electrode length), ϵ_0 is the permittivity in the vacuum, and r_{in} and r_{out} are the inner and outer radii of the barrier respectively. Unlike C_b , the calculation of C_g is not easy because of the complex shape of the inner electrode. However, we know that C_{cell} obeys:

$$\frac{1}{C_{cell}} = \frac{1}{C_g} + \frac{1}{C_b}, \quad (6)$$

so through the determination of C_{cell} the C_g is obtained. The equivalent capacity of the cell can be extracted from the charge versus voltage plot (Lissajous figure). The Lissajous plots for different applied voltages are presented in Figure 4, where the slope of the top and bottom lines give C_{cell} . Additionally, the slopes of the right and left sides (which correspond to plasma on-times) indicate the effective capacitance of discharge ($C_{cell} \leq C_{eff} \leq C_b$) which equals C_b when the gap is completely filled with plasma (homogenous plasma free of nondischarge zones). In Figure 4 Lissajous plots have been obtained for discharges created with voltages having three different peak-to-peak amplitudes. It also presents the Q-V plot for dielectric barrier capacitance ($C_b = 22.13$ pF). It can be seen from the figure that bottom and top lines of all Lissajous plots, whose slopes present the C_{cell} , are the

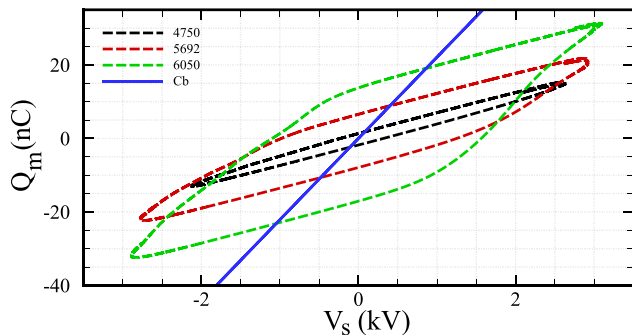


FIGURE 4 Lissajous plots at three different applied voltages compared with $C_b = 22.13$ pF. Gas flow and voltage frequency are fixed at 50 ml/min and 72 kHz, respectively.

same as expected, and they give a value of 6 pF for C_{cell} . Having determined the net capacitance of cell, the discharge gap capacitance (C_g) can be determined based on Equation (6), resulting in $C_g = 8.23$ pF. As mentioned before, the slope of left and right lines of the Lissajous plots indicates the effective capacitance that only equals C_b when the reactor gap is completely discharged. Comparing the slopes of these lines with C_b reveals that with increasing the voltage amplitude, the effective capacitance tends toward the barrier capacitance. For the plot showing a peak-to-peak voltage 6050 V, the slope of these lines are same as the slope of the Q-V plot for C_b , which implies that the DBD is fully discharged and plasma fills all zones in the gap (uniform plasma) for this applied voltage.

Given the values of C_b , C_g , and C_m , Equations (1) and (2) can be solved with measured profiles I_m , V_m , and V_s to calculate the plasma voltage, plasma current, and other plasma parameters, as shown in Figure 5, where time evolution of the parameters are illustrated at $V_{pp} = 5692$ V and gas flow 50 ml/min. Figure 5A compares the measured voltages V_m and V_s with calculated voltages V_p and V_b . Notice that the V_m value is in the range of volts while three other voltages are in the kV range. This is because most of the voltage drop occurs within the reactor and only a small amount of applied voltage reaches the monitoring capacitor. The relation $V_s = V_p + V_b + V_m$ is well-established, as expected. The current profiles in Figure 5b reveal that there is a phase difference between net current and both plasma current and gap current. The sum of the two branch currents equals the net measured current. The maximum value of both branch currents is smaller than the maximum value of net current, implying that for the duration of plasma ignition, the displacement current (I_g) is not zero and there are some nondischarged zones on the surface of the electrodes which behave as small capacitors and establish a displacement current. Figure 5c,d illustrate the reduced electric field (E_g/N), electron energy (ϵ_e), total electric charge (Q), and electron density (n_e) profiles. They indicate that during a voltage period there are two gas breakdowns, one of which is stronger than the other. When the reduced electric field is higher the electron density is low and vice versa, because the higher reduced electric field is achieved when there is less electric charge inside the gap to shield the background electric field of the electrode.

Figure 6 shows the effect of voltage amplitude variation on plasma parameters such as power consumption, the reduced electric field in the gap, electron energy, and electron density. According to the figure, an increase in voltage amplitude leads to an increase in power consumption and electron density. The increase in power

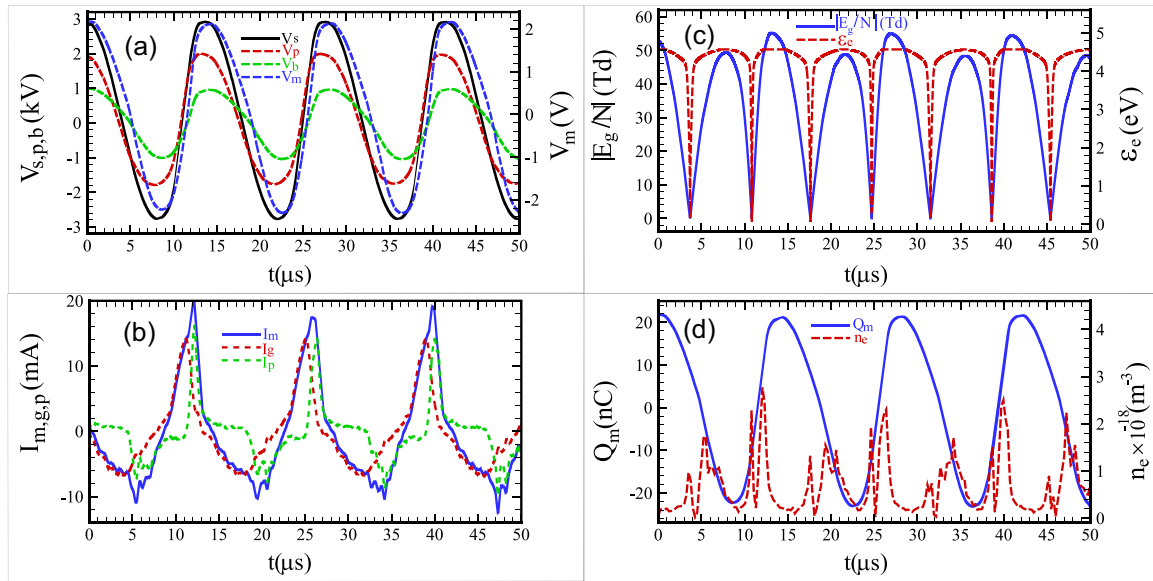


FIGURE 5 Measured and calculated plasma parameters for $V_{pp} = 5692$ V and gas flow 50 ml/min. The voltages (a), the electric currents (b), the electron energy and the electric field (c), and the electric charge and the electron number density (d).

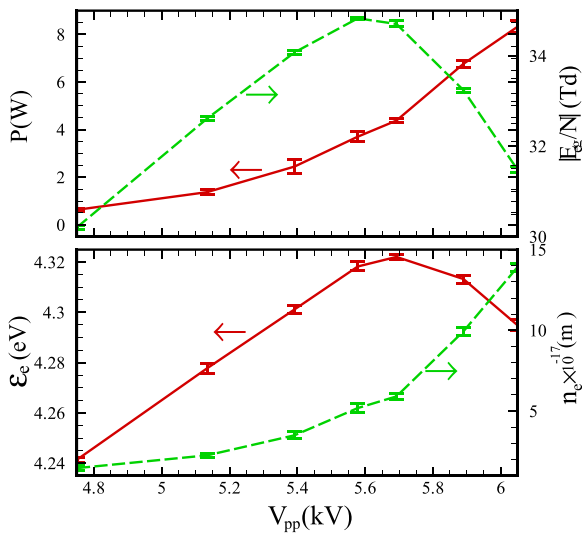


FIGURE 6 The effect of voltage on power consumption, reduced electric field, electron energy, and electron density, averaged over one voltage period at gas flow 50 ml/min.

and electron density for different voltage ranges is not the same; at higher voltages a small increase in voltage leads to a significant increase in power and electron density, while in a lower voltage range they are not significantly affected by a change in voltage. Unlike the electron density and power consumption, which increase continuously with an increasing applied voltage amplitude, electron energy and electric field peak at $V_{pp} \approx 5.65$ kV. Electron energy and electric field increase with an increase in voltage from 4.8 to 5.65 kV, however, they experience a decrease in value when the voltage

increases over the range from 5.65 to 6 kV. By more increasing applied voltage the density of charged species (electron and ions) increases due to high rate of ionization. When density of charged species is enough high the plasma sheath formation and charge accumulation effect near electrodes are established. Plasma sheath and charge accumulation attenuate intensity of the background electric field of electrodes. Therefore, net electric field of discharge gap will be smaller than background field of electrodes. In higher voltages the charge accumulation near electrodes is more stronger and it attenuates the background electric field more vigorously. Therefore, increase of voltage from $V_{pp} = 5.6$ kV decreases the net electric field of discharge gap. This decrease in electric field by increasing the applied voltage in high voltages continues until the background electric field of electrodes becomes more bigger than the electric field of the sheath. In the case of electron energy, it is dependent to electric field and is determined by the Boltzmann equation, so it shows the same behavior as the electric field shows.

3.2 | The gas heating and conversion

OES was applied to determine which active species were formed in the methane DBD. Figure 7 presents the emission spectrum of pure methane for applied voltage $V_{pp} = 5692$ V and flow rate 50 ml/min. The detailed emission lines of main species are listed in Table 1.

Even though the detailed chemical or electrical processes are unknown, the rotational temperature has

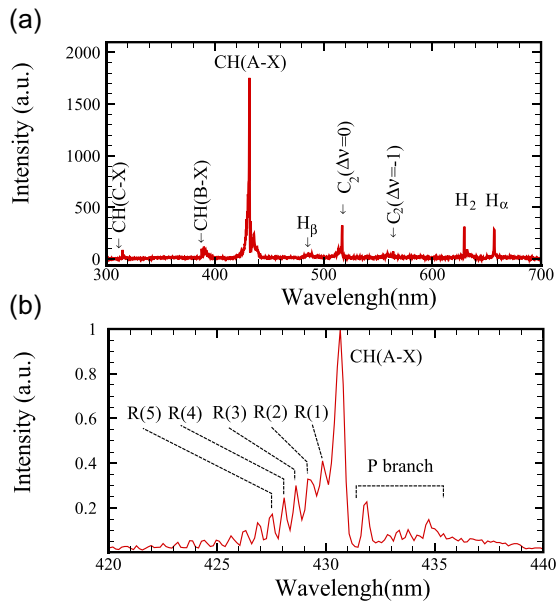


FIGURE 7 Optical emission spectrum of methane DBD at $V_{pp} = 5692$ V and gas flow 50 ml/min for spectral range from 300 to 700 nm (a) and 420 to 440 nm (b).

TABLE 1 Spectroscopic features of the main species observed in CH_4 plasma

Species	Transition	$\Delta\vartheta$	Wavelength (nm)
CH(C-X)	$C^2\Sigma^+ \rightarrow X^2\Pi$	0	314.3
CH(B-X)	$B^2\Sigma \rightarrow X^2\Pi$	0	388.9
CH(A-X)	$A^2\Delta \rightarrow X^2\Pi$	0	431.5
H_β	Balmer $n = 4 \rightarrow 2$	–	486.1
H_α	Balmer $n = 3 \rightarrow 2$	–	656.3
C_2	Swan $d^3\Pi_g \rightarrow a^3\Pi_u$	0	516.2
C_2	Swan $d^3\Pi_g \rightarrow a^3\Pi_u$	–1	563.2
H_2	Fulcher $d^3\Pi_u^- \rightarrow a^3\Sigma_g^+$	0	628.2

often been a reference to estimate the gas temperature in a corresponding emission region^[36]. The gas temperature, T_g , of heavy species can be deduced from the rotational temperature, T_{rot} , due to the strong coupling between translational and rotational energy states. Rotational temperature can be determined from the relative intensity ratio of the R line of the CH spectrum. The background spectrum must be substituted before measuring the relative intensity of R branches. Temperature determination based on the CH band due to $A^2\Delta \rightarrow X^2\Pi$ (431.5 nm) has been discussed for DBD in Nozaki et al.^[26]. A more detailed analysis of the rotational fine structure of this transition band presenting R lines is shown in Figure 7b, where excited

rotational lines were observed up to R(7), indicating that the gas temperature could be limited under 1000 K. Because a high-temperature heat source is required to excite to higher rotational levels, it is almost impossible to attain such high temperatures in practical DBD applications. The calculation of the rotational temperature from the rotational fine structure is well known. The Boltzmann plot method can be applied for plasmas in thermodynamic equilibrium, but also in less restrictive conditions, if the pressure is sufficiently high to establish thermal equilibration of the state populations, when the radiative decay probability of considered excited state is smaller than the collision rate of the molecules. In this condition, the rotational temperature obtained from the Boltzmann plot using rotational energy of the upper state levels can be considered to be equal with gas temperature. For low-pressure plasmas, the collisional relaxation is not sufficient to ensure the redistribution of the population levels before radiation. In this case, under the assumption of direct electronic excitation, the populations of the rotational levels of the excited state under consideration are proportional to the populations of the corresponding levels of the ground state from which the electronic excitation emanates, and the gas temperature is obtained from the Boltzmann plot using the rotational energies of the levels in the ground state^[37]. With I_{UL} being the spontaneous emission intensity of a single spectrum line of wavenumber ν , we have:

$$I_{UL} \propto S_{UL} \nu_{UL}^4 \exp\left(-\frac{E_U hc}{k_B T_{rot}}\right) \quad (7)$$

where subscripts L and U, respectively are the quantum numbers of the rotational levels in the lower and upper electronic states. The statistical weight S_{UL} denotes the line strength, and reflects the transition probability, E_U is a rotational term in the upper electronic state, k_B is the Boltzmann constant, h is Planck's constant, c is the velocity of light, and T_{rot} denotes the rotational temperature. The above equation can be as:

$$\ln\left(\frac{I_{UL}}{S_{UL} \nu_{UL}^4}\right) \propto -\frac{E_U hc}{k_B T_{rot}}. \quad (8)$$

The intensity, I_{UL} , and wavenumber, ν , were experimentally obtained, while the rotational term, E_U , and intensity factor, S_{UL} , were obtained from given formulae with careful consideration^[26]. The logarithmic plot of $\left(\ln\left(\frac{I_{UL}}{S_{UL} \nu_{UL}^4}\right)\right)$ against $(E_U hc/k_B)$ yields a straight line when local thermal equilibrium for excited CH is established; the rotational temperature can be determined from the given slope. By using this approach we

calculated the gas temperature for different voltage amplitudes and flow rates. Figure 8 presents the effects of gas flow rate and voltage on gas heating.

Figure 8 provides information on background gas heating in the methane DBD and illustrates how gas flow and applied voltage can change the background gas temperature. According to Figure 8a, minimum gas heating occurs at a flow rate of 75 ml/min with a resulting gas temperature of 504 K. An increase in flow rate from 20 to 75 ml/min decreases the gas temperature ≈ 30 K, while for flow rates of more than 75 ml/min the gas temperature is approximately constant with a value of ≈ 520 K. According to Bernoulli's Principle, an increase in the speed of fluid (gas flow) leads to a decrease in pressure. In constant total input energy, a decrease in pressure increases delivered energy density, leading to more heating of the gas. On the other hand, an increase in flow results in a decrease in residence time which means the background gas spends less time inside the plasma region (reactor), leading to less heating of the gas. These two opposite effects determine how gas temperature changes by the gas flow. Therefore, the gas temperature shows a nonlinear behavior by gas flow and a minimum temperature can happen in a typical flux, which in our work happens in flow = 75 ml/min. Figure 8b shows that at lower voltages the background gas is heated more, and with an increase in voltage amplitude the temperature of background gas decreases. Gas temperature fall with the increase of voltage is stronger at lower voltages, while at higher

voltages an increase in voltage does not change the gas temperature significantly and it remains stable. This implies that at higher voltages, a greater proportion of the input energy is used for ionization processes than is used in gas heating, which is confirmed by Figure 6 where the electron density increased with increasing voltage. If we assume that the temperature distribution in plasma region is uniform, its evolution at a constant background gas flow (constant gas velocity) is governed by following simplified energy equation:

$$\frac{\partial \rho C_p T}{\partial t} = \sum_i \vec{j}_i \cdot \vec{E} - \sum_i S_i \Delta H_i, \quad (9)$$

where first term accounts for joule heating due to acceleration of ions in the electrostatic field having current density j_i and ΔH_i is the heat of formation for reaction i having source function S_i . In voltage range considered here, from minimum voltage required for plasma ignition to voltage that full discharge happen, second term become bigger than first term by increase of input voltage. Because any extra input energy (by voltage increase) is delivered to inelastic reaction channels like ionization and dissociation, and other inelastic collisions. Therefore, the gas temperature decrease by increasing input voltage in the range considered here, as can be seen from Figure 8b.

Finally, Figure 9 represents conversion of methane gases for different gas flow rates and different input voltages. Where the conversion is calculated by the following equation:

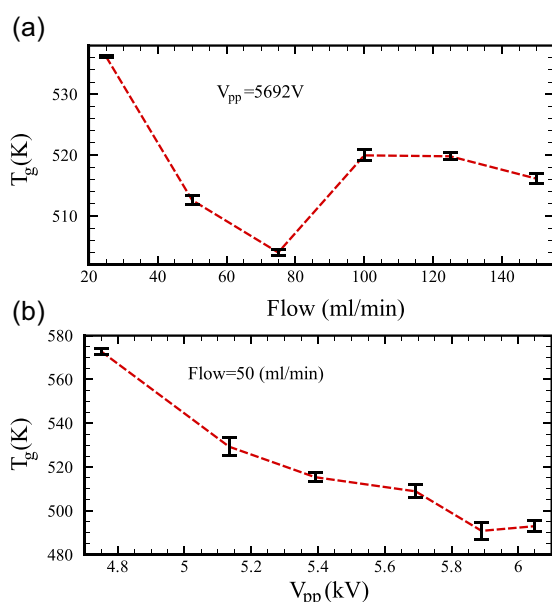


FIGURE 8 Background gas temperature as a function of gas flow (a) and voltage (b)

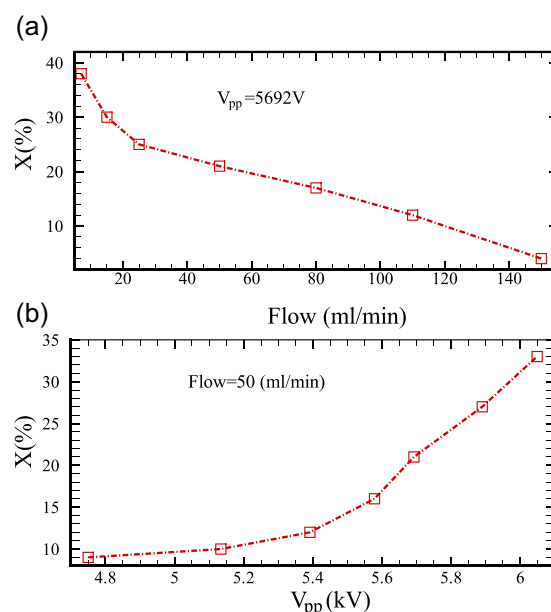


FIGURE 9 Methane gas conversion as a function of gas flow (a) and voltage (b).

$$X_{\text{CH}_4}(\%) = \frac{\text{Moles of CH}_4 \text{ converted}}{\text{Moles of CH}_4 \text{ input}} \times 100. \quad (10)$$

The figure shows that the conversion of background gases increases by increasing voltage while increase of input flow rate decreases it. Increasing input voltage increases the plasma power (see Figure 6), and it in turn enhances the energy delivered to the plasma, so dissociation and ionization reactions receive more energy, leading to higher conversion rate. With increase of gas input flow rate the resident time decreases, so background gas molecules spend less time in plasma discharge region and inside reactor and some molecules leave the reactor without any interaction with plasma species. This explains why an increase in input gas flow rate decreases the conversion.

4 | CONCLUSIONS

The electrical modeling, Boltzmann equation solver, optical emission analysis were used to investigate the effects of changeling the voltage and flow rate on plasma and gas parameters. A methane-fed DBD operant form nondischarge to full-discharge modes was employed for this study. First, the capacitance of the discharge gap and cell were determined. The plasma current and plasma voltages were calculated by electrical modeling. They were used to specify the electron density, electric field, consumed power, and electron energy by solving the Boltzmann equation. The gas temperature was determined by the Boltzmann plot approach, by considering the spectral lines of CH(A–X) species. Results showed that a uniform plasma with tunable gas temperature and plasma parameters is achievable in the DBD, which is a key factor in gas conversion applications. The fully discharge mode happened when the amplitude of applied voltage was more higher than breakdown voltage. In this mode, the estimated gas temperature was in minimum value, compared with lower voltage conditions. This uniform plasma is achieved by tuning applied voltage, gas flow, and reactor characteristics. This DBD, which creates a uniform plasma, in synergy with catalytic materials, which requires controllable heating, has the potential to show good performance in methane gas conversion. Therefore, as an outlook for the next work, we will investigate methane conversion in our DBD, whose inner wall will be coated with photocatalytic materials.

ACKNOWLEDGMENTS

The authors acknowledge funding from the European Research Council (ERC) under the European Union's Horizon 2020 research and innovation programme

(grant agreement No. 810182); ERC Synergy Grant SCOPE, Surface-CONfined fast-modulated Plasma for process and Energy intensification in small molecules conversion.

DATA AVAILABILITY STATEMENT

The data that support the findings of this study are available from the corresponding author upon reasonable request.

ORCID

Nima Pourali  <http://orcid.org/0000-0002-0962-5926>

Joe Gregory  <http://orcid.org/0000-0003-3642-3817>

Volker Hessel  <http://orcid.org/0000-0002-9494-1519>

Evgeny V. Rebrov  <http://orcid.org/0000-0001-6056-9520>

REFERENCES

- [1] P. Tang, Q. Zhu, Z. Wu, D. Ma, *Energy Environ. Sci.* **2014**, 7, 2580.
- [2] B. Wang, S. Albarracín-Suazo, Y. Pagán-Torres, E. Nikolla, *Catalysis Today* **2017**, 285, 147.
- [3] Y. Chen, X. Mu, X. Luo, K. Shi, G. Yang, T. Wu, *Energy Technol.* **2020**, 8, 1900750.
- [4] D. Li, R. Xu, Z. Gu, X. Zhu, S. Qing, K. Li, *Energy Technol.* **2020**, 8, 1900925.
- [5] H. Puliyalil, D. L. Jurković, V. D. Dasireddy, B. Likozar, *RSC Adv.* **2018**, 8, 27481.
- [6] N. Pourali, M. Sarafraz, V. Hessel, E. Rebrov, *Phy. Plasmas* **2021**, 28, 013502.
- [7] U. Kogelschatz, *Plasma Chem. Plasma Process.* **2003**, 23, 1.
- [8] N. Peters, L. Schücke, K. Ollegott, C. Oberste-Beulmann, P. Awakowicz, M. Muhler, *Plasma Processes Polymers* **2021**, 18, 2000127.
- [9] F. Paschen, Ueber die zum funkenübergang in luft: wasserstoff und kohlenensäure bei verschiedenen drucken erforderliche potentialdifferenz..., JA Barth, **1889**.
- [10] A. M. Loveless, G. Meng, Q. Ying, F. Wu, K. Wang, Y. Cheng, A. L. Garner, *Sci. Reports* **2019**, 9, 1.
- [11] R. H. Fowler, L. Nordheim, *Proc. R. Soc. London A.* **1928**, 119, 173.
- [12] A. Venkatraman, A. A. Alexeenko, *Phys. Plasmas* **2012**, 19, 123515.
- [13] D. Devia, L. Rodriguez-Restrepo, E. R. Parra, *Ingeniería y Ciencia* **2015**, 11, 239.
- [14] A. De Giacomo, V. Shakhmatov, O. De Pascale, *Spectrochim. Acta B Atomic Spectrosc.* **2001**, 56, 753.
- [15] S. Qin, A. McTeer, *Surface Coatings Technol.* **2007**, 201, 6508.
- [16] C. Seidel, H. Kopf, B. Gotsmann, T. Vieth, H. Fuchs, K. Reihls, *Appl. Surface Sci.* **1999**, 150, 19.
- [17] K. Warner, G. M. Hieftje, *Spectrochim. Acta B Atomic Spectrosc.* **2002**, 57, 201.
- [18] T. Duguet, V. Fournée, J. Dubois, T. Belmonte, *Surface Coatings Technol.* **2010**, 205, 9.
- [19] F. Peeters, T. Butterworth, Atmospheric Pressure Plasma—from Diagnostics to Applications, **2019**, p. 13.
- [20] A. Pipa, T. Hoder, J. Koskulics, M. Schmidt, R. Brandenburg, *Rev. Sci. Instrum.* **2012**, 83, 075111.

- [21] A. Pipa, J. Koskulics, R. Brandenburg, T. Hoder, *Rev. Sci. Instrum.* **2012**, 83, 115112.
- [22] S. Jo, D. H. Lee, W. S. Kang, Y.-H. Song, *Phys. Plasmas* **2013**, 20, 083509.
- [23] M. Archambault-Caron, H. Gagnon, B. Nisol, K. Piyakis, M. R. Wertheimer, *Plasma Sources Sci. Technol.* **2015**, 24, 045004.
- [24] U. Pal, A. Sharma, J. Soni, S. Kr, H. Khatun, M. Kumar, B. Meena, M. Tyagi, B. Lee, M. Iberler, et al., *J. Phys. D Appl. Phys.* **2009**, 42, 045213.
- [25] A. Y. Nikiforov, C. Leys, M. Gonzalez, J. Walsh, *Plasma Sources Sci. Technol.* **2015**, 24, 034001.
- [26] T. Nozaki, Y. Unno, Y. Miyazaki, K. Okazaki, *J. Phys. D Appl. Phys.* **2001**, 34, 2504.
- [27] H. Bai, B. Huang, Y. Liu, C. Zhang, T. Shao, *J. Phys. D Appl. Phys.* **2021**, 54, 424002.
- [28] Y.-C. Chang, P.-Y. Wu, J.-C. Jhuang, C. Huang, *J. Appl. Spectrosc.* **2021**, 88, 1067.
- [29] S. Kado, Y. Sekine, T. Nozaki, K. Okazaki, *Catal. Today* **2004**, 89, 47.
- [30] M. Liao, Y. Wang, H. Wu, H. Li, W. Xia, *Plasma Sci. Technol.* **2015**, 17, 743.
- [31] I. Akintola, G. Rivera-Castro, J. Yang, J. Hicks, D. Go, in *2022 IEEE International Conference on Plasma Science (ICOPS)*, IEEE **2022**, p. 1.
- [32] S. Suzuki, H. Sekiguchi, *J. Chem. Eng. Japan* **2010**, 43, 158.
- [33] G. Hagelaar, L. Pitchford, *Plasma Sources Sci. Technol.* **2005**, 14, 722.
- [34] H. Bahador, N. Pourali, *Phys. Plasmas* **2019**, 26, 013502.
- [35] N. Pourali, V. Hessel, E. V. Rebrov, *Plasma Chem. Plasma Process.* **2022**, pp. 1–22.
- [36] P. Bruggeman, N. Sadeghi, D. Schram, V. Linss, *Plasma Sources Sci. Technol.* **2014**, 23, 023001.
- [37] M. Heintze, M. Magureanu, M. Kettlitz, *J. Appl. Phys.* **2002**, 92, 7022.

How to cite this article: N. Pourali, K. Lai, J. Gregory, Y. Gong, V. Hessel, E. V. Rebrov, *Plasma. Process. Polym.* **2022**, e2200086.
<https://doi.org/10.1002/ppap.202200086>